Supplementary Information:

	Raman shift (cm^{-1})			
	v4	v3	v2	v1
FMO4	489.6	571.0	636.2	721.6
FMO3	470.3-500.8	571.9	636.5	728.8
FMO2	487.1	572.0	641.8	743.4
FMO1	493.1	573.0	643.0	739.2
HMO	490.2	566.9	641.1	744.9

Table S1 Active Raman modes for HMO, FMO1, FMO2, FMO3 and FMO4 obtained by peak fitting.

Material	[Mn] / mg L^{-1}
FMO1	15.8
FMO2	79.0
FMO3	120
FMO4	302

Table S2 ICP-MS results for the solution after galvanic exchange reaction of materials FMO1, FMO2, FMO3 and FMO4

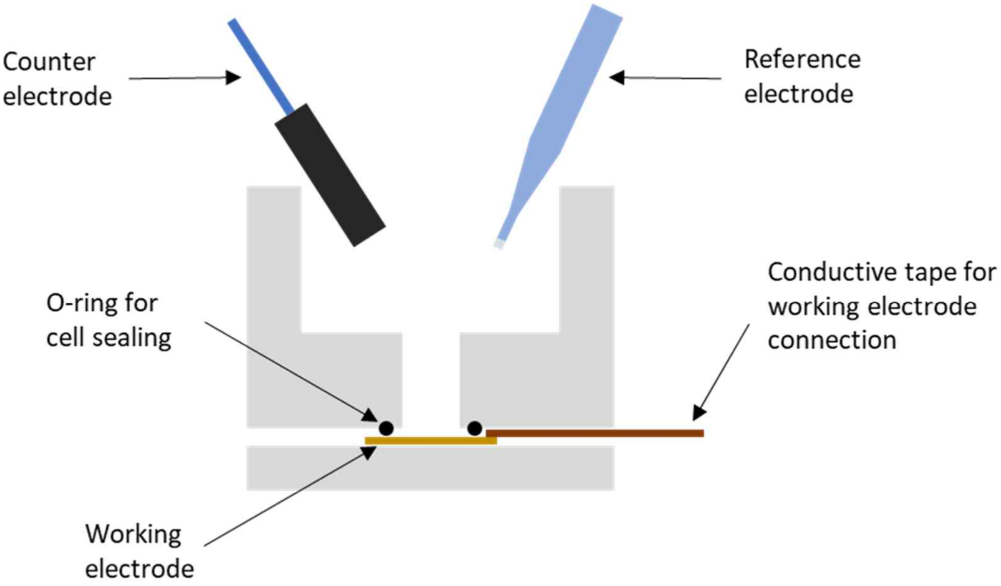

Fig. S1 Schematic of the customized Teflon-cell used to measure the CVs.

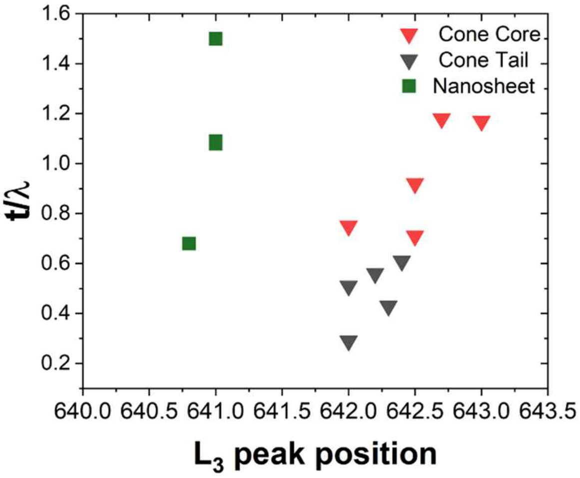

Fig. S2 Effect of the relative thickness (t/λ, where t is thickness and λ is mean free electron path) in the oxidation state evaluation of Mn oxides as shown by the shift in the Mn L_3 white line maximum. This evidences that the difference of up to 2.5 eV between nanosheet and nanocone measurements cannot solely be derived from their different thickness affecting the self-reducing effect of the electron probe. Thus, there is an intrinsic Mn oxidation state difference between nanomorphologies.

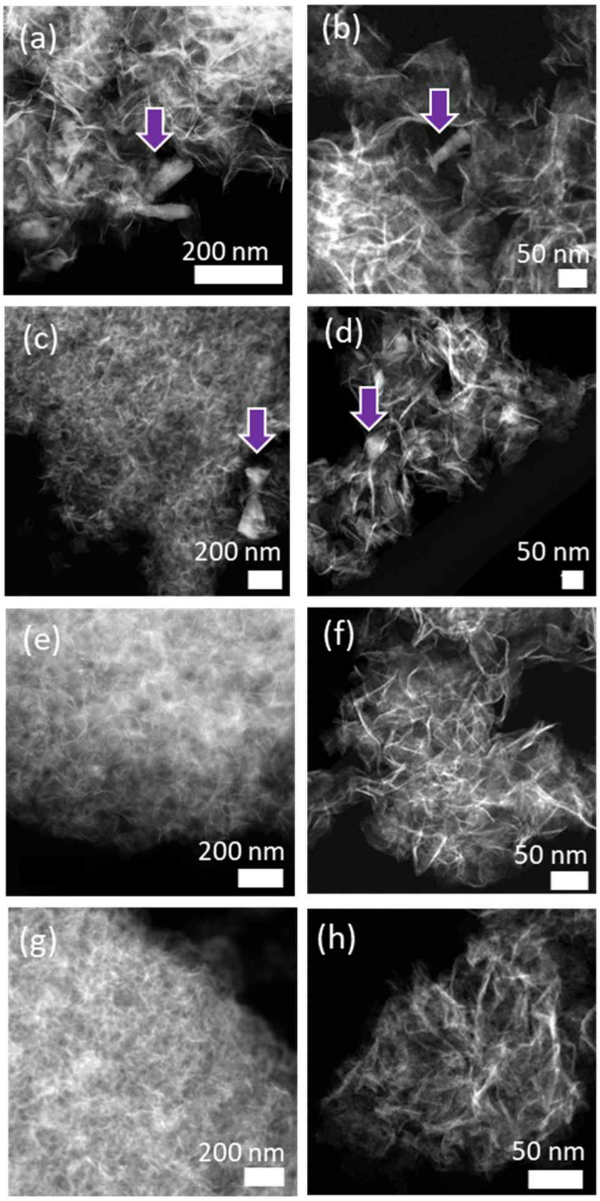

Fig. S3 STEM-HAADF micrographs of (a, b) FMO1 (c, d) FMO2 (e, f) FMO3 and (g, h) FMO4.

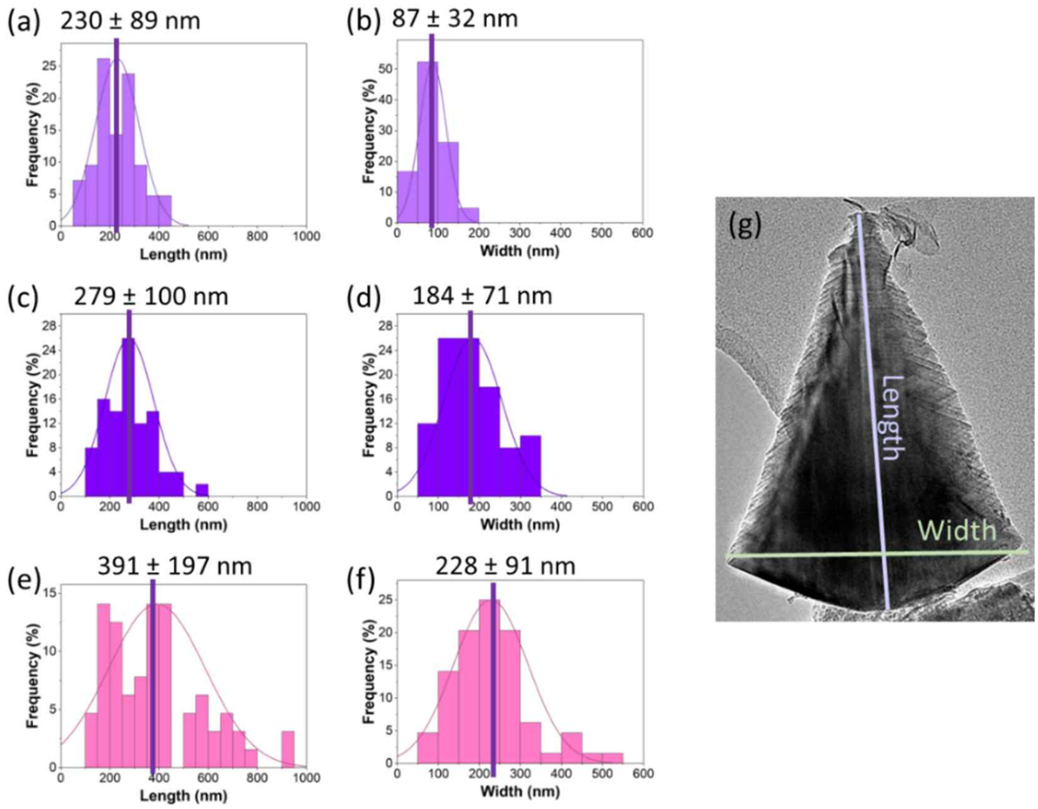

Fig. S4 Histogram distributions of the length and width of nanocones of (a, b) FMO1 (c, d) FMO2 (e, f) 1M-FMO2 (g) TEM image showing how the measurements were taken.

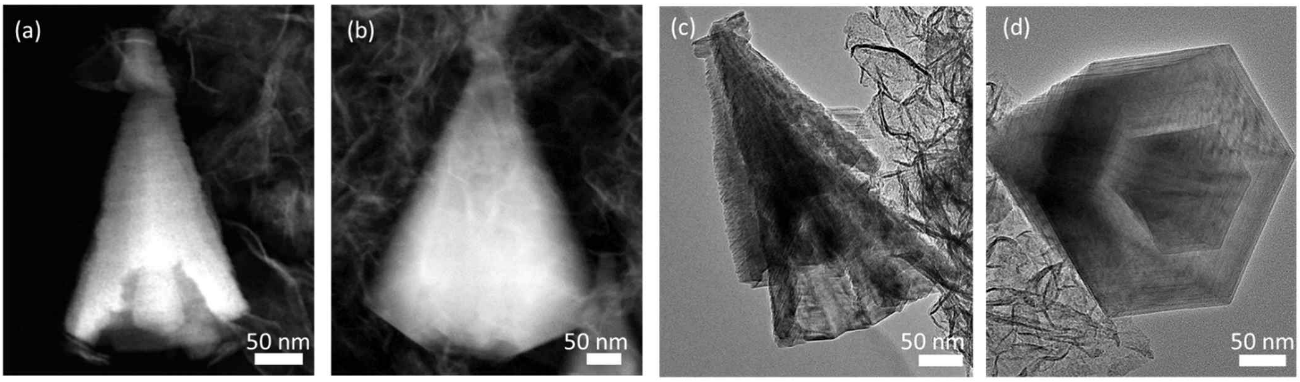

Fig. S5 STEM-HAADF micrographs of (a) hollow cone (b) closed cone. (c, d) TEM micrographs showing cones growing inside cones (pyramidal growth) from two different projections.

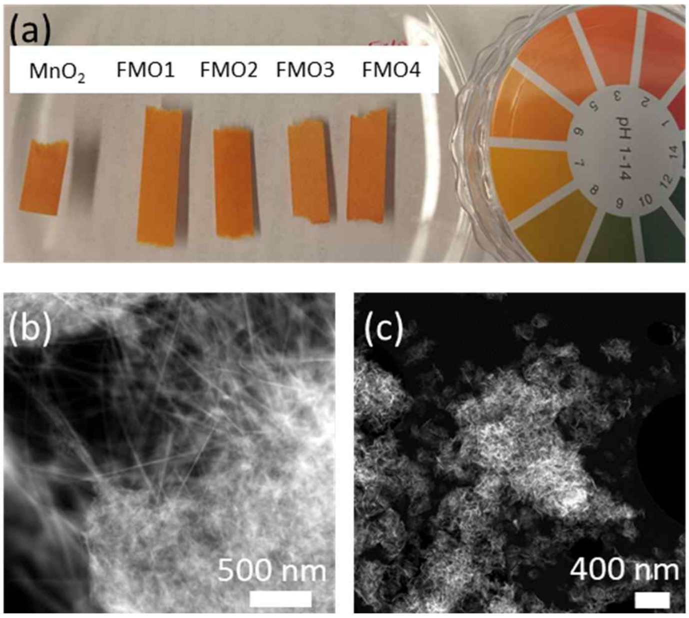

Fig. S6 (a) pH measures of the MnO_2 solution and the Fe^{2+} solutions used for the synthesis of FMO1, FMO2, FMO3 and FMO4. (b) MnO_2 nanowires obtained from galvanic exchange reaction using FMO3 conditions with pH adjusted to 10.5 with TMAOH. (c) MnO_2 nanosheets obtained from galvanic exchange reaction using FMO3 conditions with equivalent TMA^+ molarity with TMACl.

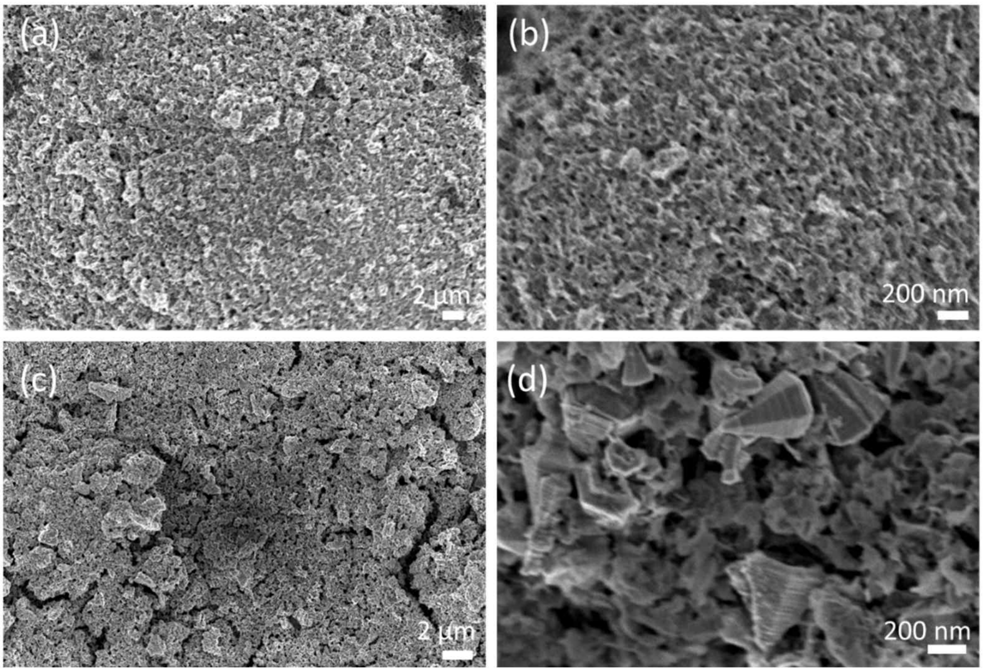

Fig. S7 SEM micrographs of (a, b) HMO electrode and (c, d) 1M-FMO2 electrode.

Capacitive behaviour of FMO materials:

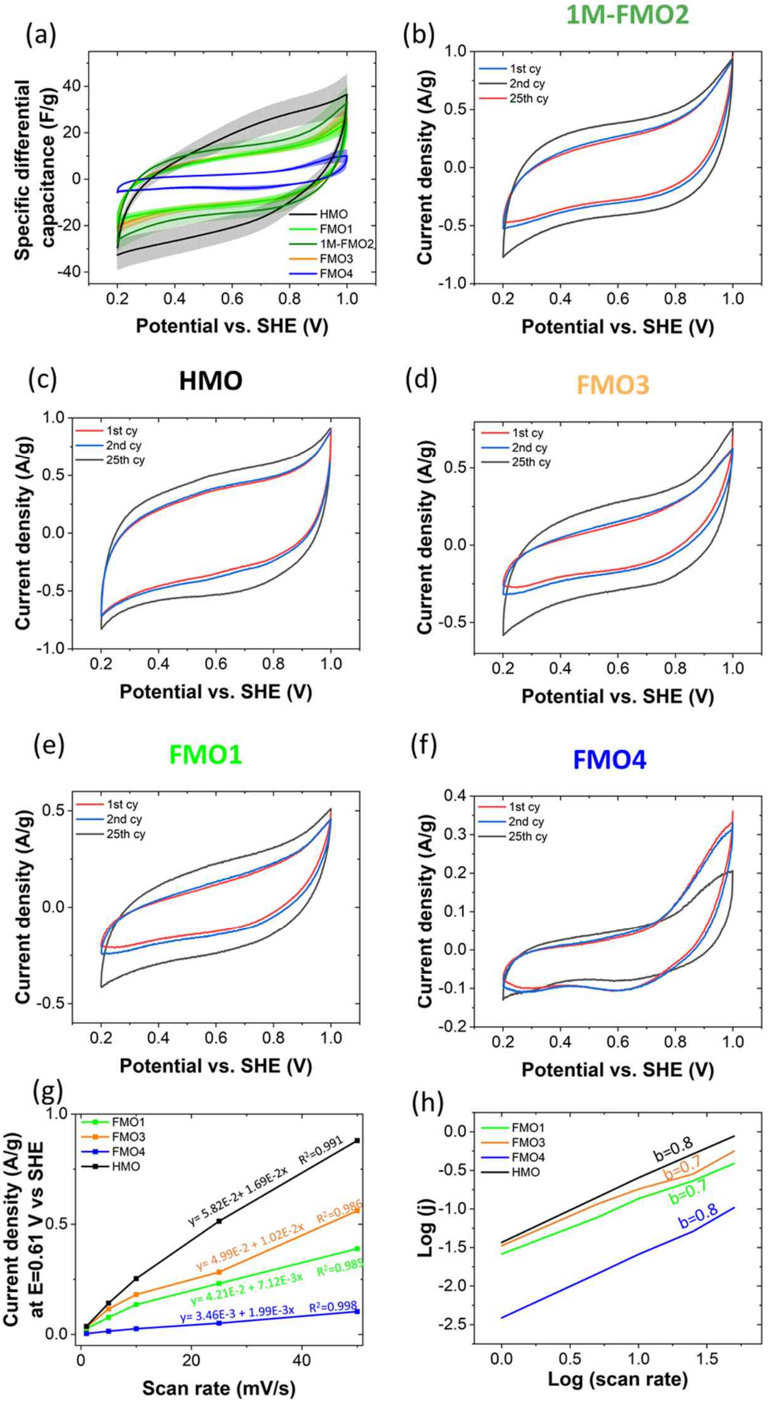

Fig. S8 (a) Differential capacitance of HMO, FMO1, 1M-FMO2, FMO3 and FMO4. (b-f) 1st, 2nd and 25th CVs of HMO, FMO1, 1M-FMO2, FMO3 and FMO4. (g) Current density (at E=0.61 V at scan rates of 1, 5, 10, 25 and 50 mV/s for HMO, FMO1, FMO3 and FMO4 materials. (h) Log-log plot of the current density versus scan rate revealing similar slope b for HMO, FMO1, FMO3 and FMO4.

Fig. S8a shows the differential capacitance of HMO, FMO1, 1M-FMO1, FMO3 and FMO4. The capacitance follows the trend HMO>1M-FMO2>FMO1≈FMO3>FMO4, thus showing a general tendency of decreasing capacitance with Fe content. Although Fe doping on birnessite MnO_2 can improve the capacitance of these materials by enhancing their conductivity, a too high Fe content produces the opposite effect due to an increased number of boundaries derived from smaller grain sizes[9]. This is the case for FMO materials, where Raman spectroscopy and HRTEM observations confirmed a significant decrease in grain size with Fe incorporation, particularly for FMO3 and FMO4 materials.

Beyond the presence of nanocones and different Fe contents, other factors can play a role in the capacitive behavior of FMO materials, such as the different oxidation state of Mn in the precursor MnO_2 materials (HMO and 1M-HMO). This could account for the difference in capacitance of 1M-FMO2 and FMO1.

Some insights of the effect of Mn oxidation state on the mechanisms of charging could be gained from the evolving shape of the CV curves when comparing the 1st, 2nd and 25th CVs of the different materials (Fig. S8b-f). It can be seen that in those with higher amounts of Fe, the first cycles show a pronounced oxidative signal at E ~ 1V. In FMO4 even a second reductive peak is visible at E ~ 0.6 V. Those peaks fade with further electrochemical cycling and the capacitance is consequently enhanced. They may indicate structural changes related to irreversible modifications in the Mn oxidation states after which the material stabilizes and becomes more capacitive.

Finally, a scan rate study was performed on the different materials. A plot of current density vs. scan rate can be found in Figure S8g. Its slope can be associated to the capacitance of each material, thus confirming the trend observed in Figure S8a. For the FMO samples, the scan-rate dependency of the current seemingly changes for the higher scan rates, indicating a limitation of the capacitive mechanism. Thus, Fig. S8h shows the log-log plot of the current density vs. scan rate. The current response of pseudocapacitive oxide materials can be governed by capacitive contributions and additional diffusion-controlled electrochemical processes:

$$i = av^b$$

Where i corresponds to the current, ν to the scan rate and a and b are constants. The b value can be extracted from the slope of log-log plots. A b value of 0.5 indicates diffusion contributions to the capacitance while a value of 1.0 is characteristic for capacitive charging[2] . As seen in Fig. S8h, the independently of the Fe content of the materials and nanomorphologies present, the $Fe_xMn_{1-x}O_2$ electrodes show values of 0.7-0.8, which indicate some diffusion contributions.

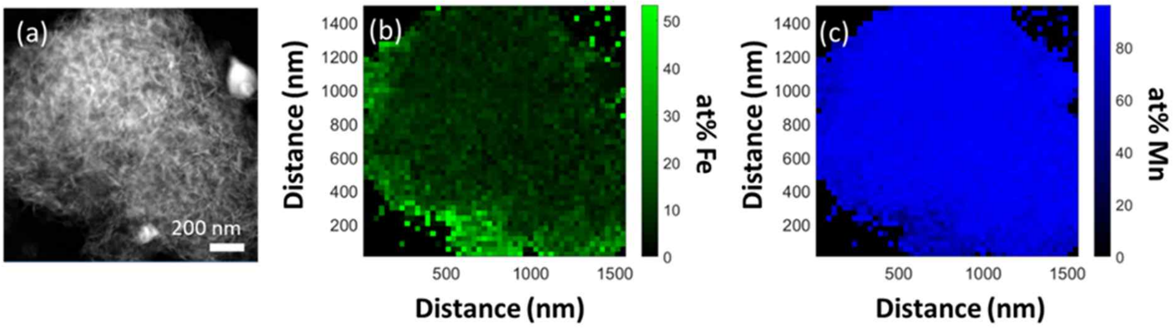

Fig. S9 (a) STEM-HAADF micrograph and corresponding EDS PCA analysis showing (b) at% Fe and (c) at% Mn of a big nanosheet aggregate. Note that the outer edges of the nanosheet assembly show a higher content of Fe.

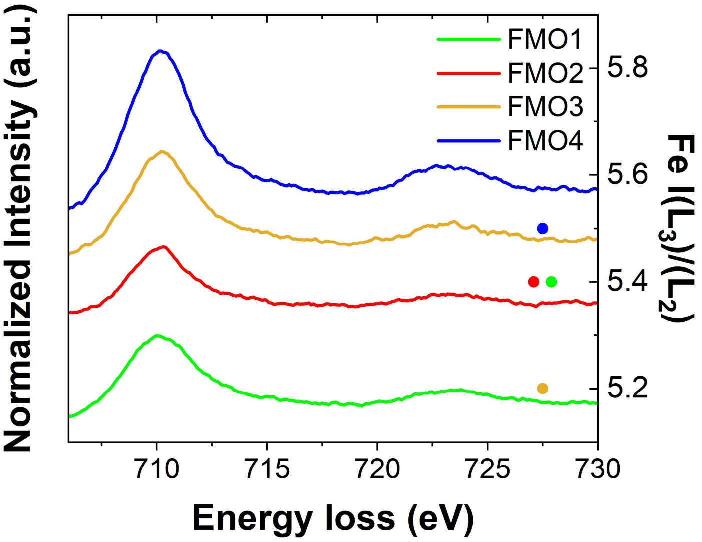

Fig. S10 Left-Y axis: Intensity of EELS Fe $L_{2,3}$ white lines of the nanosheets of each material. Right-Y axis: intensity ratio of Fe L_3 and L_2 peaks.

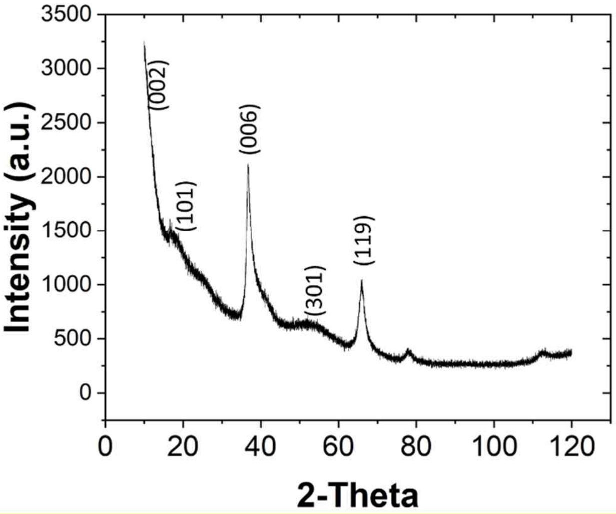

Fig. S11 XRD pattern of HMO assigned to synthetic birnessite MnO_2[3].

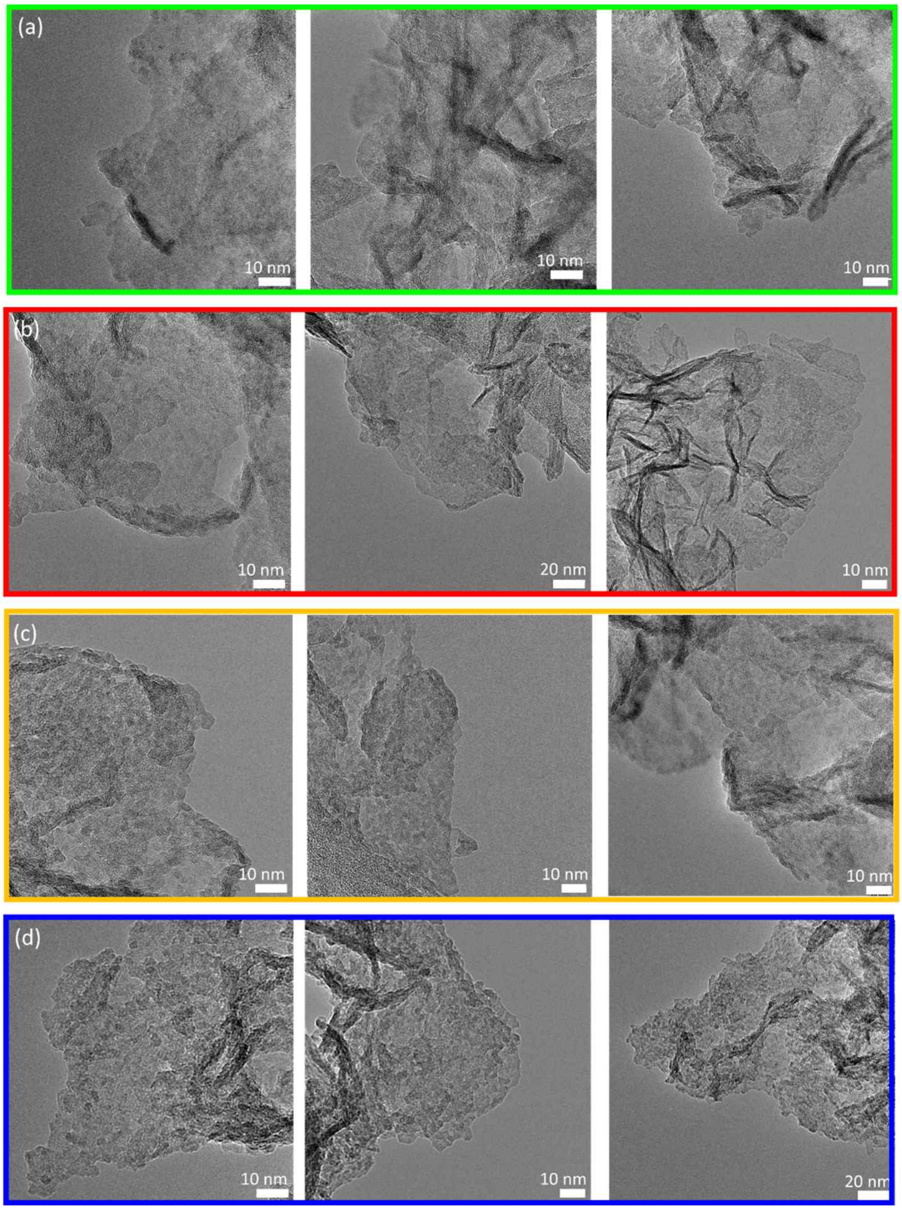

Fig. S12 TEM micrographs of nanosheets from (a) FMO1 (b) FMO2 (c) FMO3 and (d) FMO4.

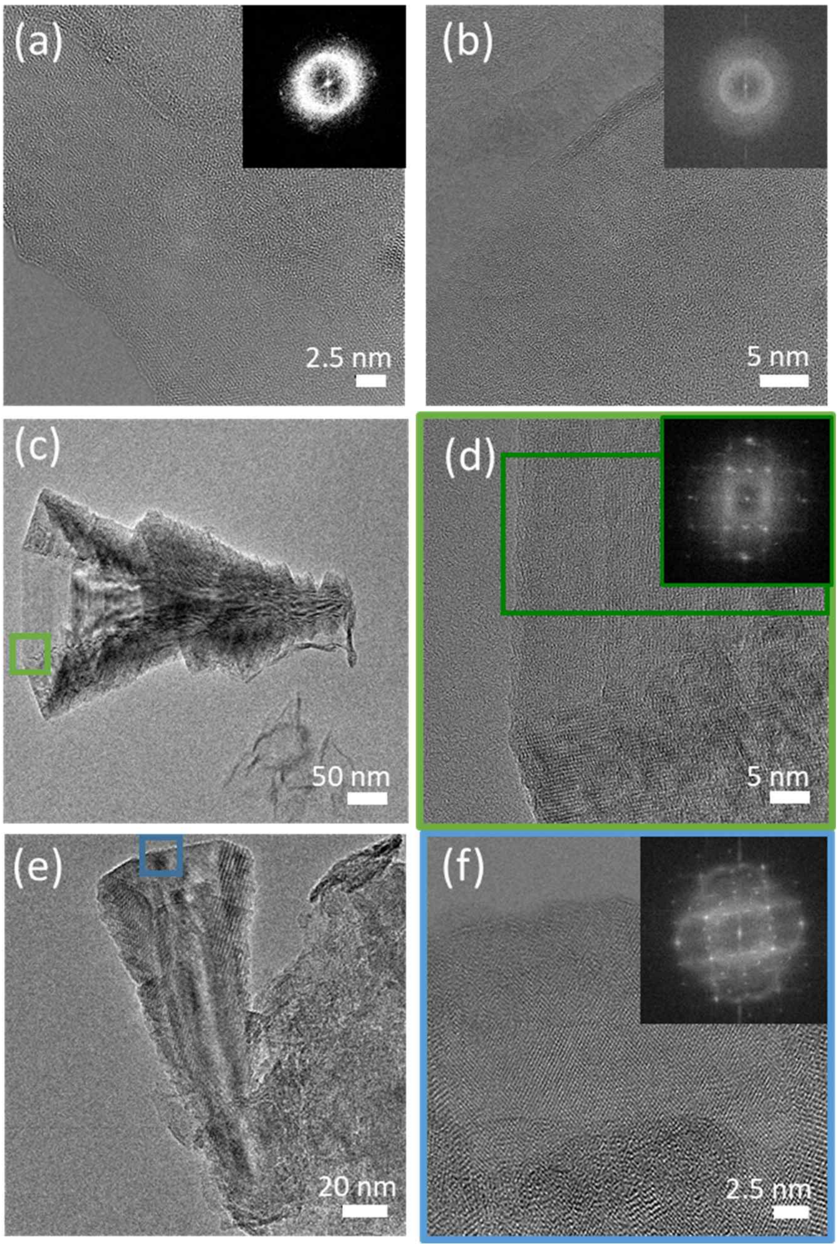

Fig. S13 Additional HRTEM images and corresponding FFT data sets for (a, b) HMO, (c-f) FMO2 nanocones to show the reproducibility of the results.

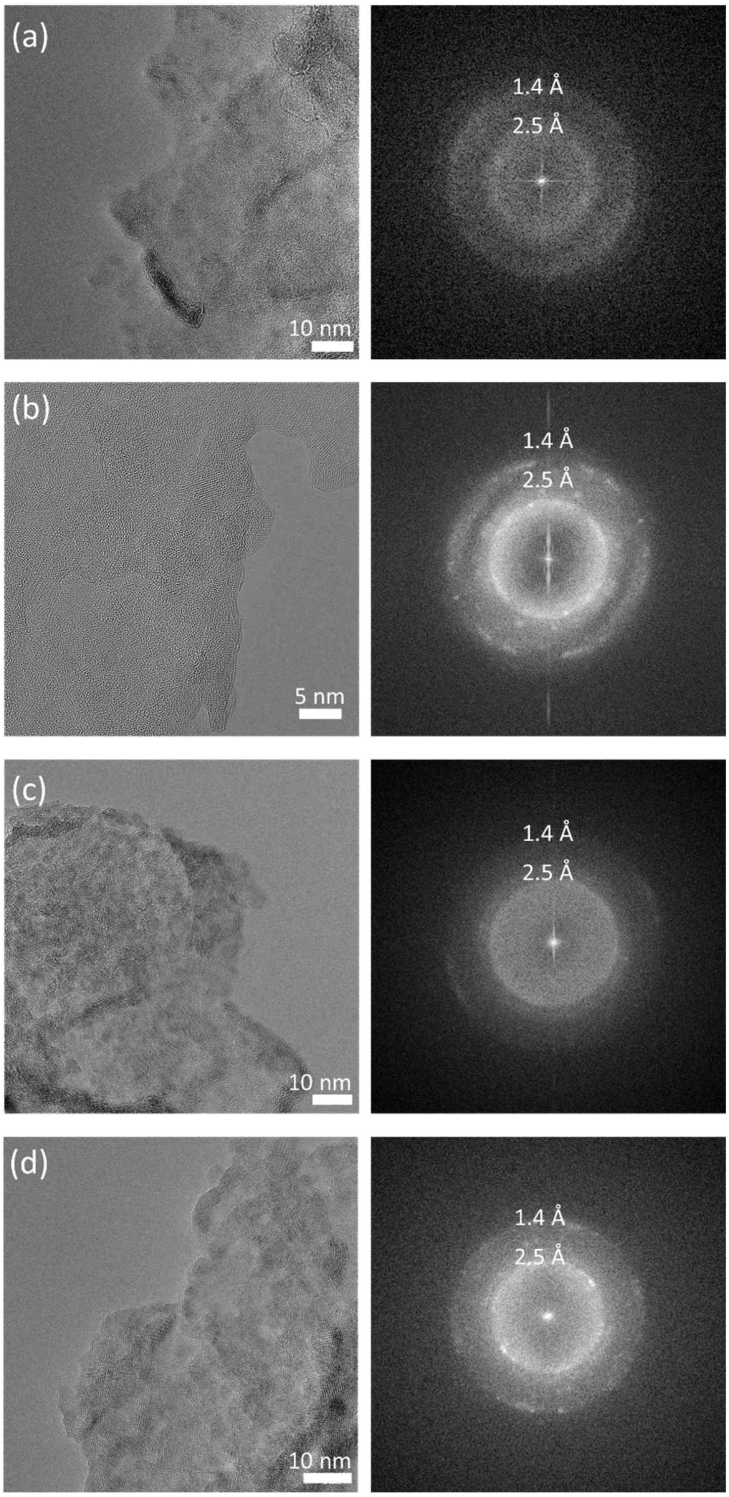

Fig. S14 HRTEM micrograph and corresponding FFT pattern of a (a) FMO1 (b) FMO2 (c) FMO3 and (d) FMO4 nanosheet, showing the same pattern than that of HMO.

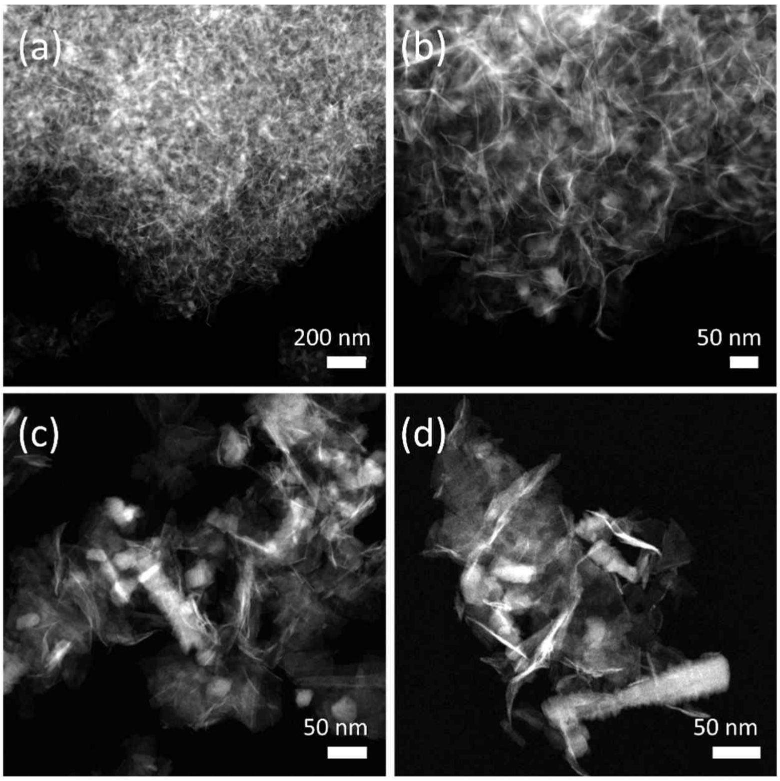

Fig. S15 (a-d) STEM-HAADF micrographs of MMO2 material synthesized using Mn^{2+} instead of Fe^{2+} in FMO2 conditions. Note that there are small round-shaped particles and elongated faceted particles instead of nanocones.

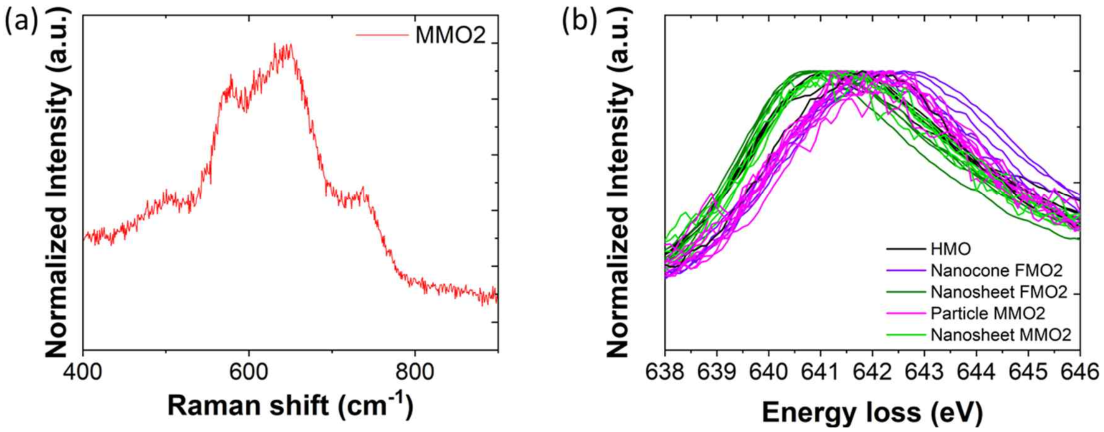

Fig. S16 (a) Raman spectra for MMO2 (b) EELS Mn L_3 spectra comparing the oxidation state of HMO nanosheets, FMO2 nanosheets and nanocones and MMO2 nanosheets and particles.

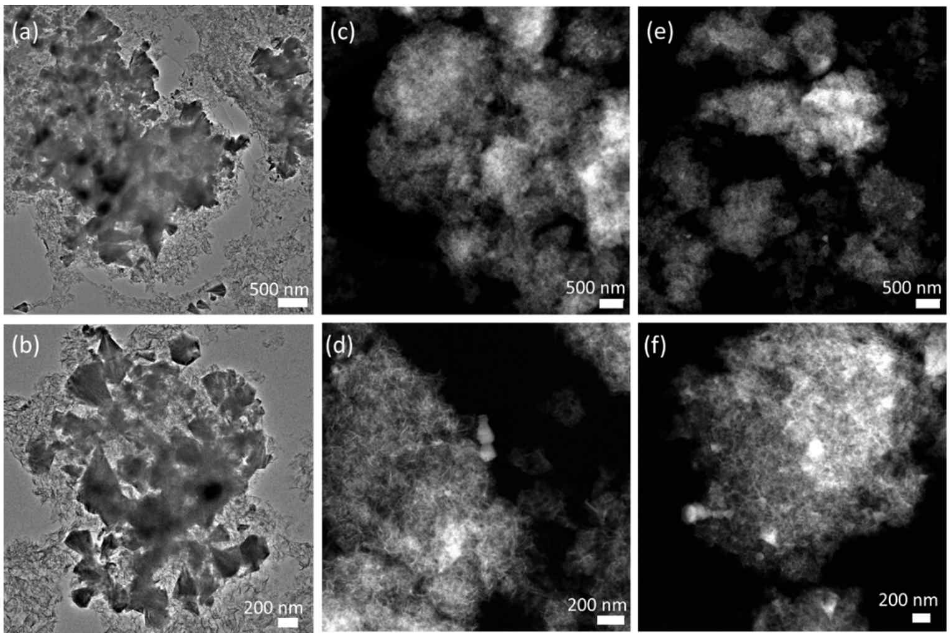

Fig. S17 (a, b) TEM micrographs of 1M-FMO2 (c, d) STEM-HAADF micrographs of 2M-FMO2 (e, f) STEM-HAADF micrographs of 3M-FMO2

References:

[1] H. Liu, W. Gu, B. Luo, P. Fan, L. Liao, E. Tian, Y. Niu, J. Fu, Z. Wang, Y. Wu, G. Lv and L. Mei, *Electrochim. Acta*, 2018, **291**, 31-40.

[2] J. Wang, J. Polleux, J. Lim, and B. Dunn, *J. Phys. Chem. C* 2007, **111**, 14925–14931.

[3] Bricker et al., *Am. Mineral.,* 1965, **50**, 1296-1354